

# Hybrid FeNiOOH/ $\alpha$ -Fe<sub>2</sub>O<sub>3</sub>/Graphene Photoelectrodes with Advanced Water Oxidation Performance

Attila Kormányos,\* Egon Kecsenovity, Alireza Honarfar, Tönu Pullerits, and Csaba Janáky\*

In this study, the photoelectrochemical behavior of electrodeposited FeNiOOH/Fe<sub>2</sub>O<sub>3</sub>/graphene nanohybrid electrodes is investigated, which has precisely controlled structure and composition. The photoelectrode assembly is designed in a bioinspired manner where each component has its own function: Fe<sub>2</sub>O<sub>3</sub> is responsible for the absorption of light, the graphene framework for proper charge carrier transport, while the FeNiOOH overlayer for facile water oxidation. The effect of each component on the photoelectrochemical behavior is studied by linear sweep photovoltammetry, incident photon-to-charge carrier conversion efficiency measurements, and long-term photoelectrolysis. 2.6 times higher photocurrents are obtained for the best-performing FeNiOOH/Fe<sub>2</sub>O<sub>3</sub>/graphene system compared to its pristine Fe<sub>2</sub>O<sub>3</sub> counterpart. Transient absorption spectroscopy measurements reveal an increased hole-lifetime in the case of the Fe<sub>2</sub>O<sub>3</sub>/graphene samples. Long-term photoelectrolysis measurements in combination with Raman spectroscopy, however, prove that the underlying nanocarbon framework is corroded by the photogenerated holes. This issue is tackled by the electrodeposition of a thin FeNiOOH overlayer, which rapidly accepts the photogenerated holes from Fe<sub>2</sub>O<sub>3</sub>, thus eliminating the pathway leading to the corrosion of graphene.

## 1. Introduction


Photoelectrochemical (PEC) solar fuel generation is considered as a potential one-step strategy to store the energy of sunlight

Dr. A. Kormányos, E. Kecsenovity, Prof. C. Janáky  
Department of Physical Chemistry and Materials Science  
University of Szeged  
Szeged H-6720, Hungary  
E-mail: attila.kormanyos@chem.u-szeged.hu; janaky@chem.u-szeged.hu

A. Honarfar, Prof. T. Pullerits  
Chemical Physics and NanoLund  
Lund University  
Box 124 Lund 22100, Sweden

Prof. C. Janáky  
ELI-ALPS  
ELI-HU Non-Profit Ltd.

Wolfgang Sandner utca 3, Szeged H-6728, Hungary

 The ORCID identification number(s) for the author(s) of this article can be found under <https://doi.org/10.1002/adfm.202002124>.

© 2020 The Authors. Published by WILEY-VCH Verlag GmbH & Co. KGaA, Weinheim. This is an open access article under the terms of the Creative Commons Attribution-NonCommercial License, which permits use, distribution and reproduction in any medium, provided the original work is properly cited and is not used for commercial purposes.

DOI: 10.1002/adfm.202002124

in the form of chemical bonds.<sup>[1]</sup> Design of semiconductor (SC)-based nanocomposite materials has come to the forefront of research during recent years. In these studies, the various elementary steps of the PEC process—such as light absorption (exciton formation), the transport, and transfer of the photogenerated charge carriers—can be separated.<sup>[2–4]</sup> This approach is inspired by natural photosynthesis where CO<sub>2</sub> and H<sub>2</sub>O is converted into chemicals in a complex, multi-step process (each of them facilitated by different subsystems) using the energy of sunlight.<sup>[5]</sup> This strategy seems necessary, since no single material was discovered so far, which would simultaneously fulfill all requirements that are necessary to drive PEC processes (such as hydrogen evolution, CO<sub>2</sub> reduction, and water oxidation) efficiently and cost-effectively.<sup>[6,7]</sup>

One of the most extensively studied n-type SC photoelectrodes is hematite ( $\alpha$ -Fe<sub>2</sub>O<sub>3</sub> denoted as Fe<sub>2</sub>O<sub>3</sub> in the following), due to its narrow bandgap ( $E_{BG} = 2.0$ – $2.2$  eV), and appropriate valence band (VB) position to drive the PEC water oxidation process.<sup>[8–11]</sup> Additionally, it is non-toxic, abundant, and stable in alkaline solutions.<sup>[12–14]</sup> Although, a maximum of 16.8% solar-to-hydrogen conversion efficiency can be calculated from the bandgap,<sup>[8,15]</sup> real device performances are still far behind.<sup>[16]</sup> The low charge carrier mobility ( $<1$  cm<sup>2</sup> V<sup>-1</sup> s<sup>-1</sup>),<sup>[13]</sup> and short charge carrier lifetime<sup>[15]</sup> together result in small charge carrier diffusion length (2–4 nm).<sup>[17,18]</sup> This means that the majority of photogenerated charge carriers are lost before they could reach the substrate in the electrolyte solution. On top of this, low absorption coefficient<sup>[19]</sup> and sluggish water oxidation kinetics further limits the efficiency of the overall PEC process.

Several strategies have been employed to overcome these issues, among which doping and nanostructuring are the two most prominent. For example, doping of Fe<sub>2</sub>O<sub>3</sub> with various elements—such as Si,<sup>[20]</sup> Ti,<sup>[13]</sup> Mo,<sup>[21]</sup> and Sn<sup>[22]</sup>—can significantly increase the charge carrier mobility and concentration. Nanostructured hematite architectures improved the relative volume of the space-charge layer in comparison to the bulk, which resulted in reduced charge carrier recombination and thus in higher photocurrents.<sup>[23]</sup> One very interesting approach is the combination of hematite with plasmonic gold nanohole array, which resulted in a tenfold increase of the

**Table 1.** PEC performance of state-of-the-art hematite photoelectrodes and PEC performance of the best electrodeposited hematite photoelectrodes.

Name	Synthesis method	Photocurrent density	IPCE ( $\lambda = 500$ nm)	Ref.
$\alpha$ -Fe <sub>2</sub> O <sub>3</sub> nanorods with TiO <sub>2</sub> overlayer and Co-Pi catalyst	Chemical bath deposition	6 mA cm <sup>-2</sup> at 1.23 V vs RHE in 1 M KOH, 100 mW cm <sup>-2</sup> AM 1.5G illumination	≈5%	[41]
Ru-doped $\alpha$ -Fe <sub>2</sub> O <sub>3</sub> nanorods	Doctor blading	5.7 mA cm <sup>-2</sup> at 1.23 V versus RHE in 1 M NaOH, 100 mW cm <sup>-2</sup> AM 1.5G illumination	43%	[42]
Interconnected $\alpha$ -Fe <sub>2</sub> O <sub>3</sub> nanosheets with Ag NPs and Co-Pi	Anodization	4.68 mA cm <sup>-2</sup> at 1.23 V versus RHE in 1 M NaOH, 100 mW cm <sup>-2</sup> AM 1.5G illumination	≈10%	[43]
Nanostructured $\alpha$ -Fe <sub>2</sub> O <sub>3</sub> with IrO <sub>2</sub> NPs	Atmospheric pressure chemical vapor deposition	≈3 mA cm <sup>-2</sup> at 1.23 V versus RHE in 1 M NaOH, 100 mW cm <sup>-2</sup> AM 1.5G illumination	≈22%	[23]
Nanostructured $\alpha$ -Fe <sub>2</sub> O <sub>3</sub>	Electrodeposition	1.6 mA cm <sup>-2</sup> at 1.6 V versus RHE in 1 M NaOH, 100 mW cm <sup>-2</sup> AM 1.5G illumination	–	[44]
Nanostructured Zn-, and Ti-doped $\alpha$ -Fe <sub>2</sub> O <sub>3</sub>	Electrodeposition	1.5 mA cm <sup>-2</sup> at 1.23 V versus RHE in 1 M NaOH, 100 mW cm <sup>-2</sup> 300 W Xe lamp	≈2.5%	[13]
Nanostructured Ti-, and Zr-doped $\alpha$ -Fe <sub>2</sub> O <sub>3</sub> with Co(NO <sub>3</sub> ) <sub>2</sub>	Electrodeposition	≈0.6 mA cm <sup>-2</sup> at 1.23 V versus RHE in 1 M KOH, 100 mW cm <sup>-2</sup> AM 1.5G illumination	≈3%	[19]

PEC performance compared to a low-performing bare hematite sample.<sup>[24]</sup>

SCs can be combined with various nanostructured carbon materials (such as graphene<sup>[25]</sup> or carbon nanotubes)<sup>[26]</sup> to facilitate the separation and transport of the photogenerated charge carriers, leading to enhanced PEC behavior. An additional advantage of this synergistic combination is the improved photostability of the hybrids compared to their pristine SC counterparts.<sup>[26]</sup> This concept has been already applied for various inorganic SC, such as ZnO,<sup>[27]</sup> TiO<sub>2</sub>,<sup>[28]</sup> BiVO<sub>4</sub>,<sup>[29]</sup> and Cu<sub>2</sub>O,<sup>[25,26]</sup> etc. There are also few examples, where Fe<sub>2</sub>O<sub>3</sub> was combined with nanocarbons, such as reduced graphene oxide,<sup>[30–32]</sup> graphene,<sup>[11,33,34]</sup> carbon nanotubes,<sup>[35]</sup> and carbon quantum dots.<sup>[36]</sup> Interestingly, in most of these studies, the nanocarbon component is located on the top of the Fe<sub>2</sub>O<sub>3</sub> layer,<sup>[11,30,32]</sup> thus the enhanced PEC behavior is rooted in the passivation of the surface states of Fe<sub>2</sub>O<sub>3</sub> by the nanocarbon overlayer, thereby decreasing surface recombination. The sluggish water oxidation kinetics can be alleviated by the deposition of co-catalyst overlayers such as Co-Pi,<sup>[18]</sup> FeOOH,<sup>[37]</sup> NiOOH,<sup>[38]</sup> NiFeO<sub>x</sub>,<sup>[39]</sup> Ir,<sup>[40]</sup> and IrO<sub>2</sub>.<sup>[23]</sup> Notably, the term “co-catalyst” is used in a broader sense here, as a surface layer that helps to improve the performance of the photoelectrode. Its contribution can be either accelerating the kinetics of the water oxidation reaction; or the passivation the surface states suppressing recombination. Irrespective from the mechanism, both of these contribution results in higher photocurrent density compared to the pristine semiconductor counterpart. As a result of the complex structural-, and surface modifications, PEC performance of hematite photoelectrodes has been greatly improved over the years. The state-of-the-art systems are presented in **Table 1**.

Considering the presented improvements in the above studies, Fe<sub>2</sub>O<sub>3</sub> seems to be an ideal candidate to demonstrate the effect of the various components (e.g., dopants, conductive nanoscaffolds, co-catalyst overlayers) on the PEC performance, and to precisely identify the exact role of each component. Specifically, the charge carrier dynamics of Fe<sub>2</sub>O<sub>3</sub> has been extensively studied by both ex situ and in situ transient absorption spectroscopy (TAS) measurements.<sup>[20,45–47]</sup> Contrastingly, there are only two studies on the charge carrier dynamics of Fe<sub>2</sub>O<sub>3</sub>/nanocarbon nanocomposites,

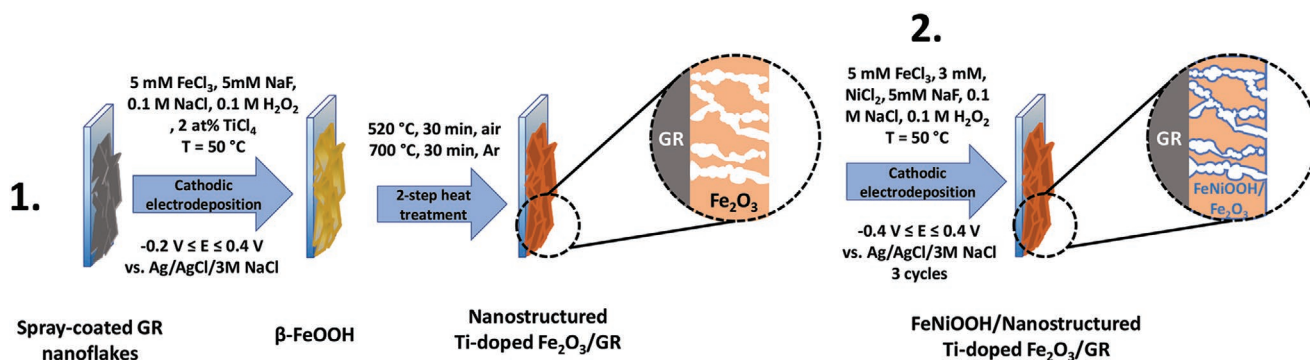
where the charge carrier lifetime was greatly increased either by the reduced graphene oxide under,<sup>[30]</sup> or graphene (GR) overlayer.<sup>[11]</sup> However, no detailed quantification of the measured data can be obtained from these reports. In general, to the best of our knowledge, there is no comprehensive study, where the effect of multiple constituents of a Fe<sub>2</sub>O<sub>3</sub> based hybrid electrodes on the charge carrier dynamics were simultaneously probed on a broad timescale. Such exercise is indeed necessary to follow all events from the charge carrier separation, through the transport, to transfer, and recombination processes.<sup>[48]</sup>

In this work we investigated the PEC behavior of FeNiOOH/Fe<sub>2</sub>O<sub>3</sub>/GR nanocomposite photoelectrodes, synthesized by electrodeposition. Electrodeposition allowed to assemble the three-component nanohybrid in a precise manner, where both structural-, and morphological attributes were carefully controlled. We investigated the effect of the Fe<sub>2</sub>O<sub>3</sub>/GR ratio as well as that of the co-catalyst loading on the PEC properties. While the highest measured photocurrent was 1.2 mA cm<sup>-2</sup> in the case of the pristine Fe<sub>2</sub>O<sub>3</sub> electrode, 2.5 and 3.1 mA cm<sup>-2</sup> photocurrents were harvested for its GR-, and co-catalyst-containing counterparts. Finally, the effect of each component on the charge carrier dynamics was identified by PEC, TAS, and intensity-modulated photocurrent spectroscopy (IMPS) measurements.

## 2. Results and Discussion

### 2.1. Electrodeposition of Fe<sub>2</sub>O<sub>3</sub>/GR Nanocomposites

The Fe<sub>2</sub>O<sub>3</sub>/GR nanocomposite photoelectrodes were synthesized in three steps: i) spray-coating of GR on FTO, ii) electrodeposition of  $\beta$ -FeOOH on GR, iii) two-step heat treatment of  $\beta$ -FeOOH/GR to yield Fe<sub>2</sub>O<sub>3</sub>/GR (**Scheme 1**). In the first step, GR nanoflakes were spray-coated on a FTO-coated glass, from their ethanol-based suspension. This process resulted in an interconnected nanocarbon network on the surface of the substrate electrode. The amount of the spray-coated GR was held constant throughout this study, namely: the electrochemically accessible surface area of GR was approximately three-times higher compared to a bare FTO electrode. Prior to the electrodeposition



**Scheme 1.** Schematic illustration of synthesis methods applied for the preparation of the nanohybrid electrodes samples: 1) cathodic electrodeposition of  $\text{Fe}_2\text{O}_3$  and 2) surface decoration with FeNiOOH co-catalyst. Detailed description of the methods can be found in the Experimental Section.

of  $\beta\text{-FeOOH}$ , a conditioning step was carried out in the electrodeposition solution to ensure the proper wetting of the GR nanoflakes and to remove any entrapped gas from the layer (potential cycling in a range where no Faradaic event occurs). This step was followed by the electrodeposition of  $\beta\text{-FeOOH}$  on the GR surface. Electrodeposition was chosen as a synthesis tool due to its beneficial features, most importantly: i) it allows high control over the thickness and morphology of the electrodeposited film, ii) it is faster compared to other synthesis methods, such as atomic layer deposition or solid state synthesis, iii) it is possible to homogeneously coat rough and complex surfaces, iv) the  $\text{Fe}_2\text{O}_3$  layer inherently deposits on the GR surface, and thus an intimate contact forms between them. The thickness of  $\text{Fe}_2\text{O}_3$  (in other words, the composition of the hybrid electrodes) was precisely tuned by varying the electrodeposition charge density. Pristine  $\text{Fe}_2\text{O}_3$  layers were also synthesized on bare FTO as a comparison. Since the thickness of  $\text{Fe}_2\text{O}_3$  can greatly influence PEC properties (e.g., insufficient light absorption for thin layers, higher degree of recombination for thicker layers) synthesis conditions were chosen in a way to make results obtained for bare  $\text{Fe}_2\text{O}_3$  and its GR-containing counterparts fully comparable. Thus, electrodeposition charge densities were normalized by the real surface area, thus the  $\text{Fe}_2\text{O}_3$  layer thicknesses were identical both in the case of the pristine and the GR-containing photoelectrodes. The final step was the heat treatment of the electrodes under air/Ar (in the case of the nanostructured electrodes) to transform  $\beta\text{-FeOOH}$  to  $\alpha\text{-Fe}_2\text{O}_3$ . All synthesis steps along with the experimental conditions are summarized in Scheme 1.

Elemental composition of  $\text{Fe}_2\text{O}_3$  surface was determined with X-ray photoelectron spectroscopy (XPS). According to the survey scans (Figure S1, Supporting Information), all  $\text{Fe}_2\text{O}_3$  samples contain Fe, O, Ti, and Sn (besides adventitious carbon). To quantify the amount of each element, high resolution scans were also recorded (Figure S2, Tables S1 and S2, Supporting Information). The surface of the  $\text{Fe}_2\text{O}_3$  sample mostly consist of O atoms (79.8 at%), which is followed by Fe (16.3 at%). The amount of Ti was around 3.0 at%. The positions of the Ti 2p peaks suggest that Ti is present in the sample as  $\text{Ti}^{4+}$ . Similar conclusions apply for Sn, which is present in as small amount as 0.9 at%. The presence of Sn can be explained by the temperature of the second heat treatment step, which allowed the diffusion of Sn from the underlying FTO to the  $\text{Fe}_2\text{O}_3$  lattice.<sup>[22,49]</sup>

Morphological characteristics of the bare  $\text{Fe}_2\text{O}_3$ , GR, and the nanocomposite films were first studied by scanning electron

microscopy (SEM). Images taken of pristine  $\text{Fe}_2\text{O}_3$  are presented in Figure S3, Supporting Information. The nanostructured  $\text{Fe}_2\text{O}_3$  layer consists of granular, oval-shaped particles, with an average size of  $\approx 100$  nm, homogeneously coating the FTO surface, similarly to precedent literature.<sup>[50,51]</sup> The GR nanoflakes covered the FTO surface (Figure 1A). The average flake size was  $1090 \pm 50$  nm. The morphology of the  $\text{Fe}_2\text{O}_3/\text{GR}$  nanocomposites strongly depended on the composition. At high  $\text{Fe}_2\text{O}_3$  loading ( $450 \text{ mC cm}^{-2}$ ), for example, the GR nanoflakes were mostly and homogeneously covered by  $\text{Fe}_2\text{O}_3$  (Figure 1B). For layers, containing less  $\text{Fe}_2\text{O}_3$  ( $Q_{\text{ED}} = 70 \text{ mC cm}^{-2}$ ) islands were formed, leaving the surface of the nanoflakes partially exposed. If the amount of  $\text{Fe}_2\text{O}_3$  was more than  $450 \text{ mC cm}^{-2}$ , all gaps among the nanoflakes were filled with  $\text{Fe}_2\text{O}_3$ , showing a similar morphology as in the case of the pristine  $\text{Fe}_2\text{O}_3$  photoelectrode. To estimate the average layer thickness ( $Q_{\text{ED}} = 450 \text{ mC cm}^{-2}$ ) of both systems, cross-section SEM images were recorded (Figure S4, Supporting Information), which revealed layer thicknesses of  $220 \pm 40$  and  $440 \pm 90$  nm for the  $\text{Fe}_2\text{O}_3$  and  $\text{Fe}_2\text{O}_3/\text{GR}$  films, respectively.

Transmission electron microscopy (TEM) images further confirmed the composite formation, as both the  $\text{Fe}_2\text{O}_3$  nanocrystals and the underlying GR nanoflakes are visible (Figure 1D–F). HR-TEM revealed lattice fringes in the case of the  $\text{Fe}_2\text{O}_3$  nanoparticles, suggesting high crystallinity all the way to the edges of the particles. Interplanar spacings of 0.370 and 0.260 nm were determined, corresponding to the [012] and [110] lattice planes of  $\alpha\text{-Fe}_2\text{O}_3$ , respectively.<sup>[50]</sup>

Figure 2A compares the Raman spectra recorded for the  $\text{Fe}_2\text{O}_3/\text{GR}$  nanocomposite sample and its pristine components. All Raman-active bands are present on the spectrum of GR (Figure 2A, blue curve; Table S3, Supporting Information).<sup>[52]</sup> The small D/G ratio (0.158) and the position of the 2D band ( $2688 \text{ cm}^{-1}$ ) implies that few-layer graphene flakes are present in our samples.<sup>[52]</sup> In the case of the  $\text{Fe}_2\text{O}_3$  film (Figure 2A, red curve) five out of the seven characteristic bands can be identified, further confirming the chemical nature of the deposit. Bands centered at 220 and  $504 \text{ cm}^{-1}$  are corresponding to the  $A_{1g}$  modes, while the ones, appeared at 288, 401, and  $613 \text{ cm}^{-1}$  are originated from the  $E_g$  modes of  $\alpha\text{-Fe}_2\text{O}_3$ .<sup>[53]</sup> Since  $\text{Fe}_2\text{O}_3$  is an antiferromagnetic material, collective spin movement can be excited in it (this is called a magnon). The band centered at  $1315 \text{ cm}^{-1}$  corresponds to a two-magnon scattering,

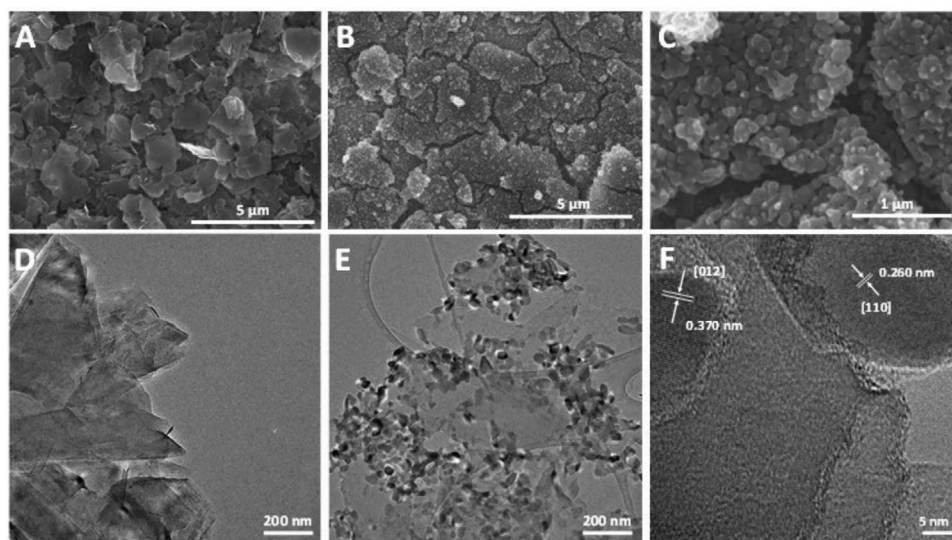


**Figure 1.** SEM images captured for A) GR-coated FTO, B)  $\text{Fe}_2\text{O}_3/\text{GR}$  nanocomposite photoelectrode ( $Q_{\text{ED}} = 450 \text{ mC cm}^{-2}$ ), and for C) the same sample as (B) at higher magnification. TEM images taken for D) GR nanoflakes, E)  $\text{Fe}_2\text{O}_3/\text{GR}$  nanocomposite ( $Q_{\text{ED}} = 450 \text{ mC cm}^{-2}$ ), and F) for the same sample as (E) at higher magnification.

which appeared from the interaction of two magnons created on antiparallel close spin sites.<sup>[54]</sup> As for the  $\text{Fe}_2\text{O}_3/\text{GR}$  nanocomposite electrode, all bands assigned both to GR and  $\text{Fe}_2\text{O}_3$  are present on the spectrum (Figure 2A, red curve). Moreover, the presence of the  $\text{D}+\text{D}'$ ,  $2\text{D}$ ,  $\text{D}+\text{D}'$ , and  $2\text{D}'$  bands in the nanocomposite is a direct proof that GR did not get oxidized during the synthetic procedure.<sup>[55]</sup> Finally, Raman bands of  $\text{Fe}_2\text{O}_3$  are slightly (an average of  $5 \text{ cm}^{-1}$ ) blue-shifted in the nanocomposite, implying an interaction between GR and  $\text{Fe}_2\text{O}_3$ .

## 2.2. Optical and Photoelectrochemical Properties

Optical properties of  $\text{Fe}_2\text{O}_3$  and  $\text{Fe}_2\text{O}_3/\text{GR}$  films were studied by UV-vis spectroscopy (Figure 2B). Three absorption features can be observed on the spectrum of bare  $\text{Fe}_2\text{O}_3$ , originating from the ligand  $d-d$  and from the direct  $\text{O}2\text{p} \rightarrow \text{Fe}4\text{s}$  transitions.<sup>[47,56]</sup> As for  $\text{Fe}_2\text{O}_3/\text{GR}$ , the only difference is a non-characteristic absorption, shifting the baseline throughout the whole spectral

range.<sup>[57]</sup> Tauc analysis was performed (Figure 2C),<sup>[58,59]</sup> and indirect bandgaps of 2.11 and 2.12 eV were calculated, in good agreement with literature values.<sup>[60]</sup>

To estimate PEC water oxidation performance, linear sweep photovoltammograms (LSV) were recorded in 1 M NaOH solution (Figure 3A). Three major conclusions can be promptly made by looking at these photovoltammograms: i) significantly higher photocurrents were harvested in the case of the GR-containing layer, ii) dark currents start to develop earlier, and iii) the onset potential slightly shifted ( $\approx 200 \text{ mV}$ ) toward more positive potentials in the case of the nanocomposite sample. This last phenomenon can be explained by the difference between the interfaces with the underlying FTO electrode surface. While the  $\text{Fe}_2\text{O}_3/\text{FTO}$  is a semiconductor/semiconductor junction, the  $\text{Fe}_2\text{O}_3/\text{GR}$  contains a semiconductor/metal interface. In addition, the temperature of the second heat treatment step ( $700 \text{ }^\circ\text{C}$ ) is high enough for Sn to diffuse into the  $\text{Fe}_2\text{O}_3$  structure, thus additionally doping it (see XPS results below). According to the literature, this slightly shifts onset potentials as well as increases the photocurrent.<sup>[22,49]</sup> The

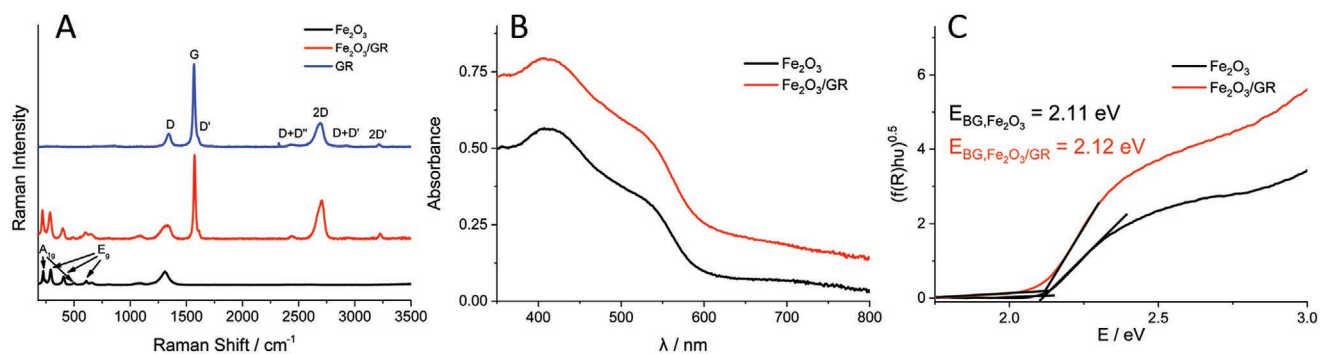


**Figure 2.** A) Raman spectra recorded for  $\text{Fe}_2\text{O}_3$ , GR and  $\text{Fe}_2\text{O}_3/\text{GR}$  thin films.  $Q_{\text{ED}}$  was  $450 \text{ mC cm}^{-2}$  in both cases. B) UV-vis spectra recorded for  $\text{Fe}_2\text{O}_3$  and  $\text{Fe}_2\text{O}_3/\text{GR}$  thin films. Similar compositions were used as for (A). C) Tauc plots constructed from diffuse reflectance spectra recorded for  $\text{Fe}_2\text{O}_3$  and  $\text{Fe}_2\text{O}_3/\text{GR}$  thin films.



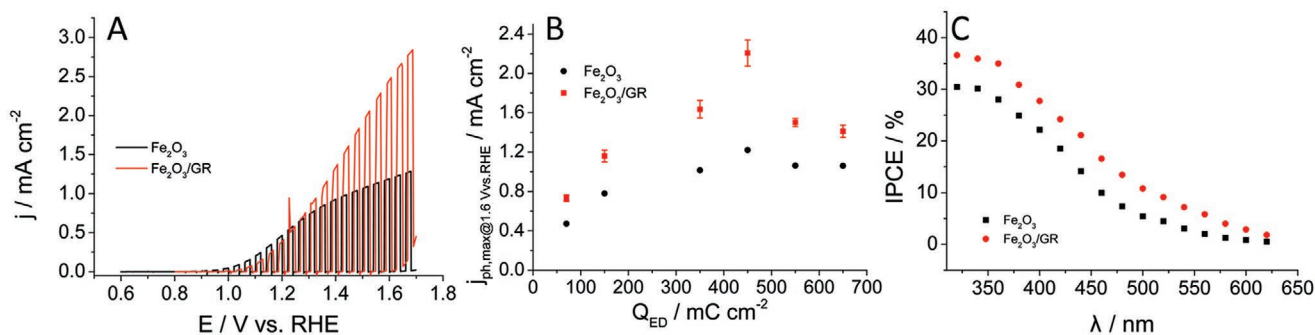


**Figure 3.** A) Photovoltammograms recorded for  $\text{Fe}_2\text{O}_3$  and  $\text{Fe}_2\text{O}_3/\text{GR}$  films in 1 M NaOH under  $100 \text{ W cm}^{-2}$  simulated AM 1.5 solar light.  $Q_{\text{ED}} = 450 \text{ mC cm}^{-2}$ ,  $\nu = 2 \text{ mV s}^{-1}$ ,  $f_{\text{illumination}} = 0.1 \text{ Hz}$ . B) Maximum photocurrents read from the set of photovoltammograms presented in Figure S5, Supporting Information. Error bars were calculated from at least three individual measurements on different electrodes. C) IPCE curves recorded for  $\text{Fe}_2\text{O}_3$  and  $\text{Fe}_2\text{O}_3/\text{GR}$  photoelectrodes in 1 M NaOH solution, applying 1.5 V versus RHE bias potential.  $Q_{\text{ED}} = 450 \text{ mC cm}^{-2}$ .

presence of GR nanoflakes in the electrode architecture hampers such a diffusion process.

The PEC behavior of nanohybrid electrodes of six different compositions was studied (Figure S5, Supporting Information). A maximum of  $1.2 \text{ mA cm}^{-2}$  photocurrent was measured for  $\text{Fe}_2\text{O}_3$  layers (Figure 3B), which value is in the range of the best-performing photoelectrodes prepared by electrodeposition.<sup>[19,50,61]</sup> Most importantly, all  $\text{Fe}_2\text{O}_3/\text{GR}$  nanocomposite photoelectrodes greatly outperformed their pristine  $\text{Fe}_2\text{O}_3$  counterparts. A maximum trend can be observed as a function of  $\text{Fe}_2\text{O}_3$  loading, both for the pristine and the GR-containing system. Two times higher photocurrents were measured compared to the bare  $\text{Fe}_2\text{O}_3$  ( $2.5$  vs  $1.2 \text{ mA cm}^{-2}$ ) for nanocomposite layers with the optimal composition ( $Q_{\text{ED}} = 450 \text{ mC cm}^{-2}$ ). To the best of our knowledge, no electrodeposited  $\text{Fe}_2\text{O}_3$ -based photoelectrode showed such PEC behavior so far (see Table 1 for comparison).

Figure 3C shows the photoaction spectra recorded for the best-performing  $\text{Fe}_2\text{O}_3$  and  $\text{Fe}_2\text{O}_3/\text{GR}$  photoelectrodes. The characteristics of the two curves are similar, with higher incident photon-to-charge conversion efficiency (IPCE) values in the case of the nanocomposite electrode. IPCE curves were integrated across the AM 1.5G solar spectrum (Figure S6, Supporting Information). The integrated maximum photocurrent values are very close to the ones measured in the photovoltammetry experiments (Table S4, Supporting Information), which further confirms the validity of the recorded photocurrent values. The IPCE values are comparable to the ones, obtained for Ti-doped hematite layers by others,<sup>[62]</sup> but a higher bias was applied in this study ( $1.5 \text{ V vs RHE}$ ). The cutoff region of the two curves are similar ( $E_{\text{cutoff}} \approx E_{\text{BG}} \approx 2 \text{ eV}$ ), indicating that the wavelength range of photoactivity has not broadened in the case of the  $\text{Fe}_2\text{O}_3/\text{GR}$  photoelectrodes. This means that the origin of the enhanced PEC behavior is rooted in the enhanced charge carrier separation and transport (i.e., the enhanced non-characteristic absorption in Figure 2B does not result in any photocurrent).

To glean insights on the electrical properties of the nanohybrid electrodes, electrochemical impedance spectroscopy (EIS) measurements were performed. Figure S7, Supporting Information, shows the Nyquist plots constructed from data collected at open circuit conditions for both  $\text{Fe}_2\text{O}_3$  and  $\text{Fe}_2\text{O}_3/\text{GR}$ .

In the case of  $\text{Fe}_2\text{O}_3$ , a distinct semicircle can be identified in the high-frequency range, assigned to an electron-transfer limited process, whereas the linear part, observed in the lower-frequency range corresponds to the diffusion-limited electron-transfer process.<sup>[63]</sup> The semicircle portion has visibly shrunk in the case of the nanocomposite layers. By fitting the semicircle portion, information can be gained on the series resistance ( $R_s$ ) and on the charge transfer resistance ( $R_{\text{ct}}$ ).  $R_s$  is similar for the two systems. As for  $R_{\text{ct}}$ , one order of magnitude smaller value was calculated for the nanohybrid sample. This phenomenon has been already discussed and elucidated in the literature for other metal-oxide/nanocarbon systems:<sup>[28,64]</sup> by electrodepositing a metal-oxide on a conductive nanocarbon network, the electric conductivity of the nanocomposite layers becomes better, compared to the pristine metal-oxides. This results in improved charge carrier transport and thereby also in suppressed charge carrier recombination explaining the higher photocurrents in the case of the  $\text{Fe}_2\text{O}_3/\text{GR}$  layers.

### 2.3. Transient Absorption Spectroscopy

To understand photoinduced charge carrier dynamics in the photoelectrodes, transient absorption spectroscopy was employed. This method provides information about formation and dynamics of photoinduced charge carriers in the time range from sub-picoseconds to nanoseconds. Time-resolved transient absorption kinetics measured at  $800 \text{ nm}$  for the bare  $\text{Fe}_2\text{O}_3$ ,  $\text{Fe}_2\text{O}_3/\text{GR}$ , and for the  $\text{FeNiOOH}$  co-catalyst decorated sample, are presented in Figure 4. The loading of the  $\text{Fe}_2\text{O}_3$  layer was identical for all samples ( $Q_{\text{ED}} = 450 \text{ mC cm}^{-2}$ ) which corresponds to about  $220 \text{ nm}$  thickness. The measurements were carried out in ex situ conditions (i.e., without any electrolyte and applied bias).

Each kinetic trace was normalized to the maximum and fitted by three-exponential decay function (see Supporting Information). Results of the fitting are summarized in Table 2.

The main features of the transient absorption spectrum and the kinetics are consistent with the earlier studies (see an example for the TA spectrum of  $\text{Fe}_2\text{O}_3$  in Figure S10, Supporting Information).<sup>[45,47]</sup> After excitation, an induced negative

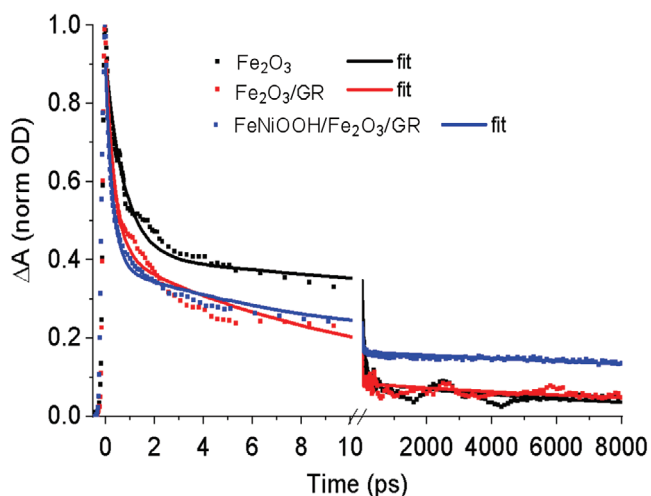


**Figure 4.** Ex situ transient absorption kinetics at  $\lambda = 800$  nm for  $\text{Fe}_2\text{O}_3$ ,  $\text{Fe}_2\text{O}_3/\text{GR}$ ,  $\text{FeNiOOH}/\text{Fe}_2\text{O}_3/\text{GR}$  photoelectrodes following  $\lambda = 400$  nm (3.1 eV) 400  $\mu\text{W}$ , 400  $\mu\text{m}$  spot diameter, 500 kHz repetition rate laser pulse excitation.  $\text{Fe}_2\text{O}_3$  loading is identical for all samples (i.e.,  $Q_{\text{ED}} = 450$   $\text{mC cm}^{-2}$ ).

absorption peak around 530 nm is due to the bleach of  $\text{Fe}_2\text{O}_3$  absorption band, and a broad positive band (which extends to the near IR region) originates from photo-generated free charges in  $\text{Fe}_2\text{O}_3$ . Interestingly, the trend observed on the decay traces for the GR-containing samples is notably comparable to its pristine and co-catalyst-coated counterparts. The TA kinetics, measured at 800 nm, have a significant sub-ps component for all samples regardless of the presence of GR or  $\text{Fe}_2\text{O}_3$  loading. The component corresponds to hot carrier cooling, which is independent of the presence of graphene. In tens of ps time range, GR leads to faster decay of the signal due to the free charges. We attribute this speeding up to the more efficient injection of charges due to the increased photoelectrode surface area provided by the graphene. Graphene can attract both holes and electrons. In contrast to the ten ps time scales, the lifetime of the ns component is somewhat prolonged due to the presence of graphene in the photoelectrode composite. Decorating the  $\text{Fe}_2\text{O}_3$  surface

**Table 2.** Fitting parameters of the transient absorption kinetics in Figure 4.

	$\text{Fe}_2\text{O}_3$	$\text{Fe}_2\text{O}_3/\text{GR}$	$\text{FeNiOOH}/\text{Fe}_2\text{O}_3/\text{GR}$
$A_1$	$0.5 \pm 0.01$ (55%)	$0.5 \pm 0.01$ (55%)	$0.5 \pm 0.02$ (58%)
$t_1$	$0.8 \pm 0.05$ ps	$0.4 \pm 0.05$ ps	$0.3 \pm 0.02$ ps
$A_2$	$0.32 \pm 0.01$ (35%)	$0.35 \pm 0.05$ (36%)	$0.2 \pm 0.04$ (24%)
$t_2$	$51 \pm 3$ ps	$10 \pm 0.5$ ps	$9.87 \pm 0.47$ ps
$A_3$	$0.08 \pm 0.01$ (10%)	$0.08 \pm 0.01$ (9%)	$0.16 \pm 0.01$ (18%)
$t_3$	$9000 \pm 1000$ ps	$14\,000 \pm 2000$ ps	$40\,000 \pm 4000$ ps

with a co-catalyst provides an additional channel to extract holes before they can recombine with the electrons. In presence of the  $\text{FeNiOOH}$  co-catalyst, the amplitude of the long nanosecond component of the charge carrier lifetime is increased to almost 20% which is significantly higher compared to the amplitude obtained for  $\text{Fe}_2\text{O}_3$  and  $\text{Fe}_2\text{O}_3/\text{GR}$ . We thereby conclude that the  $\text{FeNiOOH}$  layer effectively attracts holes from the underlying  $\text{Fe}_2\text{O}_3$  film, leading to a superior PEC performance. Similar experiments have been carried out on photoelectrodes with different compositions and very similar trends were found on the  $t_3$  values. These data further support the hypothesis made according to the photostability results (see below), that significant portion of the photogenerated holes are transported to GR, thus oxidizing it. This process can be alleviated by the proper co-catalyst coating on the surface.

#### 2.4. Photostability

To probe the photostability of the photoelectrodes, chronoamperometry measurements were carried out for two hours under continuous solar illumination (Figure 5A). While  $\text{Fe}_2\text{O}_3$  remained stable in the timeframe of the experiment, the photocurrents recorded for  $\text{Fe}_2\text{O}_3/\text{GR}$  decreased substantially within 40 min, approaching the values recorded for  $\text{Fe}_2\text{O}_3$ . It is clear from this comparison that this decrease must be tied to the degradation of the underlying GR scaffold upon applying positive bias and illumination. To probe the disappearance of GR

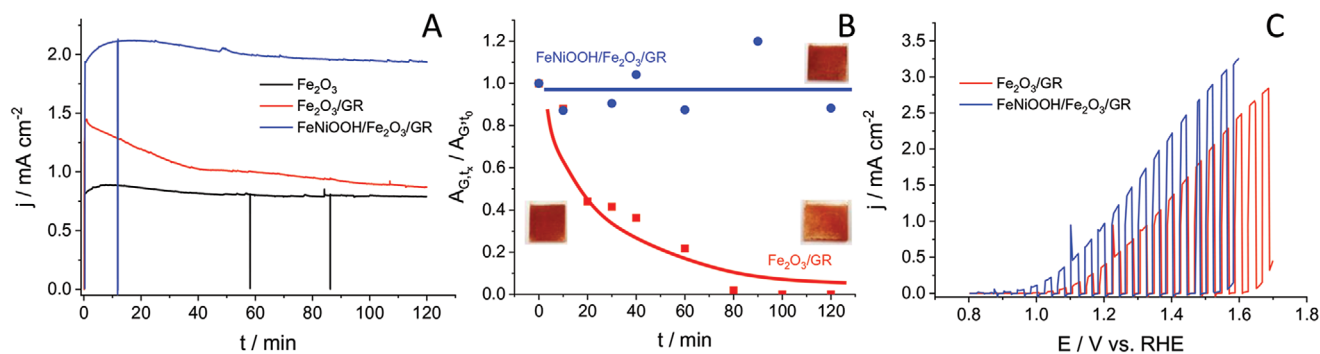


**Figure 5.** A) Long-term chronoamperometry measurements performed in 1 M NaOH solution saturated with Ar, applying  $E = 1.45$  V versus RHE potential and under  $100$   $\text{mW cm}^{-2}$  AM 1.5 simulated sunlight. The vertical lines show the current drop upon interrupting the illumination. B) Change in the normalized area of the G band of GR in time. Values were determined by integrating the G band intensity in the Raman spectra presented in Figure S8A,B, Supporting Information, and normalizing these values with area of the G band at  $t = 0$  min. Two lines were added to guide the eye of the reader. C) LSV curves recorded for  $\text{Fe}_2\text{O}_3/\text{GR}$  and  $\text{FeNiOOH}/\text{Fe}_2\text{O}_3/\text{GR}$  thin films in 1 M NaOH under  $100$   $\text{W cm}^{-2}$  simulated AM 1.5 sunlight.  $Q_{\text{ED}} = 450$   $\text{mC cm}^{-2}$ ,  $v = 2$   $\text{mV s}^{-1}$ ,  $f_{\text{illumination}} = 0.1$  Hz.

from the hybrid electrode, Raman spectra were recorded periodically (for experimental details please see Supporting Information) during the long-term photoelectrolysis experiment (Figure S8A, Supporting Information; Figure 5B). The spectra were recorded every 10 min in the first hour and every 20 min in the second hour. The presence of GR was followed by monitoring the intensity of the G band on the spectra. Clearly, this band vanished within the first hour (Figure S8A, Supporting Information). To quantify this observation, G band area was integrated for all spectra and it was normalized with the value calculated for  $t = 0$  min (Figure 5B). The normalized area of the G band decreased monotonously, and completely vanished after 80 min, confirming the disappearance of the underlying GR layer. Our observation invokes a rather uncomfortable question about the applicability of nanocarbon-containing electrodes in oxidative processes, since the widely accepted consensus is that such corrosion should not occur. There are few among the many reports on semiconductor/nanocarbon nanocomposites, however, which describe a similar effect.<sup>[65,66]</sup> Upon illumination, either the formed reactive species (OH<sup>•</sup> radicals) oxidized GR, or after charge separation, a fraction of the photogenerated holes are not transported toward the electrode/electrolyte interface, but rather to GR, which subsequently gets directly oxidized.

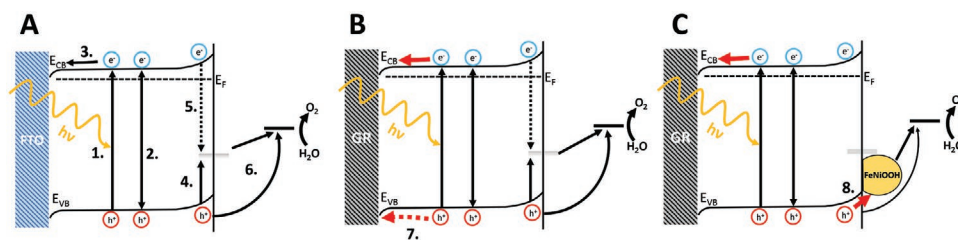
## 2.5. Synthesis and PEC Behavior of FeNiOOH/Fe<sub>2</sub>O<sub>3</sub>/GR Photoelectrodes

One viable option to tackle photostability issues is to deposit a co-catalyst layer on top of Fe<sub>2</sub>O<sub>3</sub>. By doing so, in theory, the vast majority of the photogenerated holes are rapidly transferred to the co-catalyst, which might successfully prevent the corrosion of GR. We chose amorphous mixed FeOOH and NiOOH as co-catalyst (abbreviated as FeNiOOH in the following), which was electrodeposited on Fe<sub>2</sub>O<sub>3</sub>/GR after the second heat treatment step (see Scheme 1 and the Experimental Section for further details). Both FeOOH and NiOOH are well-known water oxidation catalysts and have been widely applied as co-catalyst overlayers to boost the PEC performance of various metal oxide photoelectrodes.<sup>[37,38,67–70]</sup> In most of these studies, however, either only one of them was used<sup>[38,70]</sup> or they were deposited on top of each other as separate layers.<sup>[68,69]</sup> In our case, mixed FeOOH and NiOOH were synthesized in a single step by electrodeposition (instead of the more popular photodeposition). The main advantage of this method is that FeOOH and NiOOH are simultaneously deposited on the electrode surface and their ratio can be easily tuned by the variation of the concentration of the Fe, and Ni salts in the electrodeposition solution.<sup>[37,71]</sup> To determine the exact composition of the FeNiOOH layer, XPS measurements were performed. Survey scans proved the presence of O, Fe, and Ni in the sample (Figure S1, Supporting Information). After collecting and evaluating the high resolution scans (Figure S2, Tables S1 and S2, Supporting Information), the following elemental composition was determined: 83, 16, and 1 at% for O, Fe, and Ni, respectively. The most important conclusion from these numbers is that the Fe:Ni ratio differs from the one expected from the experimental conditions (Fe:Ni 5:3), and thus the formed coating is not stoichiometric.

Additionally, the position and intensity of the O 1s peaks suggest that O atoms in the sample are mostly in the form of hydroxide (71.0%), which is a bit more than two-times higher than in the case of the pristine Fe<sub>2</sub>O<sub>3</sub> sample. Based on this data it can be safely concluded that the electrodeposited FeNiOOH overlayer consists of mixed FeOOH and NiOOH.

Figure 5C shows LSV traces, recorded for Fe<sub>2</sub>O<sub>3</sub>/GR and its FeNiOOH-decorated counterpart. The onset potential has notably shifted to the cathodic direction (approximately 160 mV) in parallel with the 40% increase of the maximum photocurrent, reaching photocurrents as high as 3.1 mA cm<sup>-2</sup>. A notable improvement was also observed for the IPCE values, however, the wavelength-range of absorption did not change (Figure S6B, Supporting Information). The effect of the co-catalyst on the photostability of the Fe<sub>2</sub>O<sub>3</sub>/GR electrode was even more striking (blue curve in Figure 5A). The photocurrents remained stable in the course of the two-hour photoelectrolysis in contrast to the previously experienced rapid decrease. Raman spectra were also taken during this measurement (Figure S8B, Supporting Information). The G band corresponding to the presence of GR is clearly visible even at the end of the two-hour electrolysis. Data were quantified similarly as in the case of the Fe<sub>2</sub>O<sub>3</sub>/GR electrode (Figure 5B) revealing that the normalized area of the G band (thus the amount of GR in the sample) did not change significantly during the measurement. According to the PEC and Raman data, we conclude that by depositing FeNiOOH co-catalyst layer on the surface of Fe<sub>2</sub>O<sub>3</sub>/GR photoelectrode, the effect of the GR framework on the PEC properties was preserved (even slightly improved), in parallel with the protection of the underlying GR from corrosion. To further verify that the measured photocurrents are a result of PEC water oxidation, the concentration of the evolved oxygen was measured with a Clark-type O<sub>2</sub> sensor (Figure S9, Supporting Information). A Faradaic efficiency, close to 100% was calculated over the course of the three hour measurement employing a FeNiOOH /Fe<sub>2</sub>O<sub>3</sub>/GR photoelectrode.

The effect of FeNiOOH on the charge carrier transfer and recombination characteristics was further studied with IMPS.<sup>[72,73]</sup> Figure S11, Supporting Information, shows a set of IMPS spectra recorded from the FeNiOOH/Fe<sub>2</sub>O<sub>3</sub>/GR and the corresponding Fe<sub>2</sub>O<sub>3</sub> and Fe<sub>2</sub>O<sub>3</sub>/GR electrodes applying a set of potentials ranging from 0.8 to 1.55 V versus RHE. An almost perfect circle can be observed at the least positive potentials, meaning that the measured steady-state photocurrent (low frequency intercept, LFI) is close to zero, thus surface recombination dominates the PEC behavior of the system.<sup>[72]</sup> LFI shifts away from zero by the increasing potential along with the increase of the high frequency intercept (corresponding to the maximum harvestable photocurrent, if no recombination occurs). Additionally, the diameter of the semicircle in the upper quadrant, gradually decreases meaning that the applied potential has significantly influenced the equilibrium between the charge carrier transfer and recombination. In the case of the FeNiOOH-decorated sample, no semicircle can be identified in the upper quadrant above 1.4 V versus RHE, suggesting that charge carrier transfer is the dominating process.<sup>[73]</sup> The semicircle in the upper quadrant was shrunk, but never diminished in the case of both co-catalyst-less samples.



**Scheme 2.** Simplified models of the elementary processes occurring in the case of A)  $\text{Fe}_2\text{O}_3$ , B)  $\text{Fe}_2\text{O}_3/\text{GR}$ , and C)  $\text{FeNiOOH}/\text{Fe}_2\text{O}_3/\text{GR}$  photoelectrode. Elementary processes are: 1) absorption of a photon and generation of an electron-hole pair, 2) nonradiative recombination of an electron-hole pair, 3) electron transport toward the back contact, 4) trapping of holes in surface states, 5) electron-hole recombination in surface states, 6) hole-transfer from the valence band and from the surface states to the electrolyte, 7) hole-transport toward the graphene framework, and 8) hole-transport to the  $\text{FeNiOOH}$  co-catalyst overlayer.

In the following, kinetic parameters were determined from the measured IMPS spectra and plotted versus the applied potential (Figure S12, Supporting Information). Specifically, rate constants, corresponding to charge carrier transfer ( $k_{tr}$ ) and surface recombination ( $k_{sr}$ ) were determined. The  $k_{tr}$  values, calculated for the  $\text{Fe}_2\text{O}_3$  and  $\text{Fe}_2\text{O}_3/\text{GR}$  imply that GR had no obvious influence on the charge carrier transfer characteristics. On the other hand,  $k_{sr}$  values were notably higher, but only up to 1.5 V versus RHE where it drastically dropped in the case of the  $\text{Fe}_2\text{O}_3/\text{GR}$  electrode. When the  $\text{FeNiOOH}$  co-catalyst was present on the electrode surface,  $k_{tr}$  were almost identical to the ones, obtained for  $\text{Fe}_2\text{O}_3$ . This is rather peculiar, since if  $\text{FeNiOOH}$  would behave as a co-catalyst, one would expect a drastic change in the  $k_{tr}$  values. Instead of that, significantly smaller  $k_{sr}$  values were found, indicating suppressed charge carrier recombination. The effect of low  $k_{sr}$  values has also manifested in the charge transfer efficiency, thus the highest values were determined for the  $\text{FeNiOOH}/\text{Fe}_2\text{O}_3/\text{GR}$  electrode (Figure S12C, Supporting Information). From these observations one can conclude that role of  $\text{FeNiOOH}$  is to passivate the  $\text{Fe}_2\text{O}_3$  surface against recombination (reduced Fermi-level pinning and increased band-bending at the surface), rather than activating it for water oxidation. This phenomenon has been also observed and discussed in detail for  $\text{Co-Pi}$ <sup>[74]</sup> and even for  $\text{FeNiO}_x$ <sup>[39]</sup> co-catalyst overlayers.

### 3. Conclusions

We have shown that electrodeposition allows the synthesis of complex photoelectrode architectures with precisely controlled structure and composition. The photoelectrode assembly followed a bioinspired design, where the different components have different function.  $\text{Fe}_2\text{O}_3$  was responsible for light absorption, the GR framework ensured proper charge transport, while the  $\text{FeNiOOH}$  overlayer retained recombination at the surface states through passivation. Photocurrent densities were 2.6 and 1.3 times higher compared to the respective single- and two-component counterparts, and most important, exceeded all precedent literature data for electrodeposited hematite based photoelectrodes. TAS measurements revealed 1.5 times increase in hole-lifetime in the case of the  $\text{Fe}_2\text{O}_3/\text{GR}$  layers compared to the bare  $\text{Fe}_2\text{O}_3$ . Introducing a carbon component to a photoanode, however, raised an additional concern, namely that the photogenerated holes can oxidize the underlying nano-

carbon framework (as confirmed by Raman spectroscopy). By adding a third component to the system (i.e., an  $\text{FeNiOOH}$  overlayer), we were able to suppress the corrosion of the nano-carbon matrix, while all the benefits gained by the presence of GR were still present. Rate constants, corresponding to charge transfer were not affected by the presence of the co-catalyst. Contrastingly, the addition of  $\text{FeNiOOH}$  to the hematite/graphene system has greatly decreased the surface recombination. Our hypothesis of the processes occurring in the investigated systems are presented in **Scheme 2**.

For the pristine  $\text{Fe}_2\text{O}_3$ , photogenerated holes can oxidize water either directly from the valence band, or from the surface states, where they can also recombine with electrons from the conduction band (Scheme 2A). When GR nanoflakes are present (Scheme 2B), two additional processes occur: better transport of photogenerated electrons toward the back contact, due to the highly conductive nature of graphene and some of the photogenerated holes can also be transported to graphene and oxidize it (note the metallic nature of graphene). Finally, if the surface of  $\text{Fe}_2\text{O}_3$  is decorated with a material, which passivates the surface states, holes can be rapidly transported to the co-catalyst (or surface passivating agent) and to the substrate (Scheme 2C). Since the electrodeposited  $\text{FeNiOOH}$  layer is thin and porous, a small fraction of holes might be also transferred directly from the valence band of exposed hematite. Most importantly, because of the rapid hole-transfer to  $\text{FeNiOOH}$ , the pathway leading to the corrosion of graphene is successfully eliminated.

### 4. Experimental Section

**Materials:** Iron (III) chloride ( $\text{FeCl}_3$ , Sigma-Aldrich), nickel (II) chloride ( $\text{NiCl}_2$ , Sigma-Aldrich), sodium chloride ( $\text{NaCl}$ , VWR), sodium fluoride ( $\text{NaF}$ , VWR), sodium hydroxide ( $\text{NaOH}$ , VWR), potassium chloride ( $\text{KCl}$ , VWR), potassium hexacyanoferrate(II) trihydrate ( $\text{K}_4[\text{Fe}(\text{CN})_6] \cdot 3\text{H}_2\text{O}$ , Fluka), potassium hexacyanoferrate(III) ( $\text{K}_3[\text{Fe}(\text{CN})_6]$ , Reanal), sodium sulfate anhydrous ( $\text{Na}_2\text{SO}_4$ , VWR), hydrogen peroxide ( $\text{H}_2\text{O}_2$ , 30%, VWR), titanium tetrachloride ( $\text{TiCl}_4$ , Honeywell), acetone (VWR), ethanol (VWR), and graphene powder (Elicarb Premium Graphene Powder) were of analytical grade and used without further purification. Argon ( $\text{Ar}$ , 99.995%) gas was purchased from Messer. Fluorine-doped tin-oxide-coated glass (FTO, TEC15, Sigma-Aldrich) was used as a substrate. All solutions were prepared using ultrapure deionized water (Millipore Direct Q3-UV, 18.2 M $\Omega$  cm).

**Nanocomposite Synthesis:** First, the GR-dispersion ( $c = 2 \text{ mg mL}^{-1}$  in ethanol), which was sonicated for 30 min prior to use, was spray-coated



on a preheated ( $T = 140\text{ }^{\circ}\text{C}$ ) FTO electrode, using an Alder AD320 type airbrush and a homemade spray-coater robot operated with 1 bar compressed air pressure. To remove the residual traces of the solvent and to enhance adhesion of GR, the films were heat-treated in an oven at  $180\text{ }^{\circ}\text{C}$  for 1 h. The nanocarbon loading was monitored by a Mettler Toledo XPE-26 type analytical microbalance.

As a next step,  $\text{Fe}_2\text{O}_3$  was electrodeposited on the surface of the FTO or GR-coated FTO electrodes. All electrochemical syntheses and measurements were performed using an Autolab PGSTAT302 potentiostat/galvanostat. Nanostructured Ti-doped  $\text{Fe}_2\text{O}_3$  thin films were synthesized using a cathodic electrodeposition procedure adapted from the literature.<sup>[13,71]</sup> A one-compartment, three-electrode electrochemical cell was employed. FTO or GR-coated FTO was used as a working electrode, an  $\text{Ag}/\text{AgCl}/3\text{ m NaCl}$  as a reference, and a Pt sheet as a counter electrode. The deposition electrolyte solution contained 5 mM  $\text{FeCl}_3$ , 5 mM  $\text{NaF}$ , 0.1 M  $\text{NaCl}$ , 0.1 M  $\text{H}_2\text{O}_2$ , and 2 at%  $\text{Ti}^{4+}$  (added from the aqueous solution of 1 M  $\text{TiCl}_4$ ), which was gently stirred during the synthesis. To protect the spray-coated GR layer from peeling off from the FTO substrate, the concentration of  $\text{H}_2\text{O}_2$  was reduced from 1 to 0.1 M compared to the originally published recipe. Potentiodynamic electrodeposition of  $\text{Fe}_2\text{O}_3$  was carried out at  $50\text{ }^{\circ}\text{C}$  cycling the potential between  $-0.2$  and  $0.4\text{ V}$  using  $200\text{ mV s}^{-1}$  sweep rate. The thickness of the deposited thin films was controlled by the passed charge during the synthesis. After electrodeposition, thin films were thoroughly washed with deionized water and dried under air at room temperature.  $\beta\text{-FeOOH}$  was converted to crystalline  $\alpha\text{-Fe}_2\text{O}_3$  by annealing at  $520\text{ }^{\circ}\text{C}$  under air ( $\Delta T = 5\text{ }^{\circ}\text{C min}^{-1}$ ) for 30 min, which was followed by another heat treatment under Ar at  $700\text{ }^{\circ}\text{C}$  ( $\Delta T = 5\text{ }^{\circ}\text{C min}^{-1}$ ) for 30 min. The purpose of this second heat treatment step was to enhance crystallinity, and it was carried out under Ar to protect the underlying GR layer from oxidation. To characterize the coverage of GR after the synthesis a set of CVs were recorded in a solution containing 5–5 mM  $\text{K}_4[\text{Fe}(\text{CN})_6]$  and  $\text{K}_3[\text{Fe}(\text{CN})_6]$  and 1 M  $\text{KCl}$  (Figure S13, Supporting Information). Peaks corresponding to the oxidation/reduction of the  $\text{Fe}^{2+}/\text{Fe}^{3+}$  ions were clearly visible on the CV recorded for GR. No peaks were visible on the pristine  $\text{Fe}_2\text{O}_3$  electrode, while slightly higher currents could be seen in the case of the  $\text{Fe}_2\text{O}_3/\text{GR}$  sample. According to this measurement, it was concluded that the GR layer was mostly covered with  $\text{Fe}_2\text{O}_3$  after the synthesis.

**Electrodeposition of FeNiOOH on the Nanocomposite Electrodes:** To prepare FeNiOOH-decorated  $\text{Fe}_2\text{O}_3$  and  $\text{Fe}_2\text{O}_3/\text{GR}$  electrodes, a modified version of the previously described cathodic electrodeposition procedure was employed.<sup>[37]</sup> The deposition electrolyte solution contained 5 mM  $\text{FeCl}_3$ , 3 mM  $\text{NiCl}_2$ , 5 mM  $\text{NaF}$ , 0.1 M  $\text{NaCl}$ , and 0.1 M  $\text{H}_2\text{O}_2$ , stirred gently during the synthesis. The potential was cycled between  $-0.49$  and  $0.41\text{ V}$  using  $200\text{ mV s}^{-1}$  sweep rate. Temperature of the deposition solution was kept at  $50\text{ }^{\circ}\text{C}$ . Three cycles gave the highest enhancement in the PEC performance.

**Morphological and Structural Characterization:** A Hitachi S-4700 field emission SEM was operated at an accelerating voltage of 10 kV. TEM images were recorded by using a FEI Tecnai G2 20 X-Twin type instrument, operating at an acceleration voltage of 200 kV. Raman spectra were recorded on a DXR Raman Microscope using a green laser ( $\lambda = 532\text{ nm}$ ), operating at 6.25 mW laser power. UV-vis spectra were recorded on a Shimadzu UV-3600 Plus spectrophotometer in between 300 and 800 nm both in absorbance and reflectance mode. Diffuse reflectance spectra were recorded to construct the Tauc plots. XPS was performed with a SPECS instrument equipped with a PHOIBOS 150 MCD 9 hemispherical analyzer. The analyzer was in FAT mode with 40 eV pass energy (survey scans) and 20 eV pass energy (high resolution scans). The Al K $\alpha$  radiation ( $h\nu = 1486.6\text{ eV}$ ) of a dual anode X-ray gun was used as an excitation source and operated at 150 W power. Ten scans were averaged to get a single high-resolution spectrum, while 20–30 scans were averaged to get a single survey scan. The adventitious carbon peak was at 284.8 eV in all cases. For spectrum evaluation, CasaXPS commercial software package was used.

**Photoelectrochemical Measurements:** LSVs were recorded in a sealed, custom-designed one-compartment, three-electrode quartz cell.  $\text{Fe}_2\text{O}_3$ ,

$\text{Fe}_2\text{O}_3/\text{GR}$ , and  $\text{FeNiOOH}/\text{Fe}_2\text{O}_3/\text{GR}$  on the FTO substrate were used as working electrode, while a Pt sheet and  $\text{Ag}/\text{AgCl}/3\text{ m NaCl}$  were employed as counter, and reference electrodes, respectively. The applied light source was a Newport LCS-100 type solar simulator operated at full output. The radiation source was placed 18 cm away from the illuminated working electrode surface ( $100\text{ mW cm}^{-2}$  flux), which was irradiated through a quartz window. The cell contained an aqueous solution of 1 M  $\text{NaOH}$  which was saturated with Ar. Photovoltammograms were recorded using  $2\text{ mV s}^{-1}$  potential sweep in parallel with periodically interrupted irradiation (0.1 Hz). Oxygen content was monitored during long term measurements by an Orion 3 Star Clark-type oxygen sensor. Calibration of the sensor was performed in DI water, which was saturated with air for one hour and gently stirred prior to the measurement.

IPCE measurements were carried out on a Newport Quantum Efficiency Measurement System (QEPVSI-B) in a single compartment, three-electrode quartz electrochemical cell.  $\text{Fe}_2\text{O}_3$ ,  $\text{Fe}_2\text{O}_3/\text{GR}$ , and  $\text{FeNiOOH}/\text{Fe}_2\text{O}_3/\text{GR}$  on the FTO substrate were used as working electrode, while a Pt sheet and  $\text{Ag}/\text{AgCl}/3\text{ m NaCl}$  were employed as counter- and reference electrodes, respectively. The wavelength range was 300–660 nm ( $\Delta\lambda = 20\text{ nm}$  step size). The solution was 1 M  $\text{NaOH}$  saturated with Ar. The electrodes were held at 0.55 V constant potential during the measurements.

Electrochemical impedance spectra of the pristine  $\text{Fe}_2\text{O}_3$  and  $\text{Fe}_2\text{O}_3/\text{GR}$  layers were recorded in a 1 M  $\text{NaOH}$  solution saturated with Ar, at OCP, in the 0.1 Hz to 20 kHz frequency range, using a sinusoidal excitation signal (10 mV RMS amplitude). The semicircle portion of each spectrum was fitted using the Nova Software of the Autolab Instrument.

**Intensity-Modulated Photocurrent Spectroscopy:** IMPS was performed on the photoelectrodes using the same cell and electrode setup as described in the case of the photovoltammetry and IPCE measurements but using an AUTOLAB PGSTAT302N potentiostat/galvanostat equipped with an FRA32 module (Metrohm-Autolab) and a LED driver kit (Metrohm-Autolab). Spectra were recorded in the 20 kHz to 0.1 Hz frequency range applying a sinusoidal intensity modulation and bias illumination from a 470 nm blue LED. The amplitude of the modulation was 10%, while the linearity was tested and confirmed by using Lissajous plots. Normalization of the measured signal was carried out by determining the number of the incident photons employing a calibrated silicon photodiode (Thorlabs) and assuming that the LED is monochromatic at its wavelength maximum. From this, the corresponding maximum photocurrent was calculated using the assumption that one photon generates one electron–hole pair.

**Transient Absorption Spectroscopy:** Spitfire Pro (Spectra Physics) amplified laser system was used for transient absorption experiments. The excitation wavelength was 400 nm with average power 400  $\mu\text{W}$ , pulse length 100 fs, and repetition rate 500 Hz. Second harmonic of the amplifier output was generated in BBO crystal and used as pump pulses with central wavelength of 400 nm. For the probe at 800 nm the attenuated amplifier pulses were directly used. The decay traces were fitted by 3 exponential decay function as the main model for the time delayed after 50 fs by using Origin software.

## Supporting Information

Supporting Information is available from the Wiley Online Library or from the author.

## Acknowledgements

This collaborative research received funding from the European Research Council (ERC) under the EU's Horizon 2020 research and innovation program (A.K., E.K., and C.J., Grant Agreement No. 716539). ELI-ALPS is supported by the EU and co-financed by the European Regional Development Fund (GOP-1.1.1-12/B-2012-000, GINOP-2.3.6-15-2015-00001). The authors are grateful for the support from LaserLab

Europe, through campaign LLC002478]. A.H. and T.P. acknowledge financial support from Swedish Research Council and the Swedish Energy Agency. The authors thank Dr. Gergely Ferenc Samu (University of Szeged) for his help with the TA measurements in Lund and the XPS measurements in Szeged, and Dr. Báborka Janáky-Bohner for her support in the manuscript preparation.

## Conflict of Interest

The authors declare no conflict of interest.

## Keywords

composite materials, interface engineering, photoelectrochemistry, solar fuels, transient absorption spectroscopy

Received: March 6, 2020

Revised: May 7, 2020

Published online: June 25, 2020

- [1] N. Lewis, D. Nocera, *Proc. Natl. Acad. Sci. USA* **2006**, *103*, 15729.
- [2] J. Li, N. Wu, *Catal. Sci. Technol.* **2015**, *5*, 1360.
- [3] C. Janáky, K. Rajeshwar, *Prog. Polym. Sci.* **2015**, *43*, 96.
- [4] C. Janáky, E. Kecszenovity, K. Rajeshwar, *ChemElectroChem* **2016**, *3*, 181.
- [5] M. R. Wasielewski, *Chem. Rev.* **1992**, *92*, 435.
- [6] K. Rajeshwar, A. Thomas, C. Janáky, *J. Phys. Chem. Lett.* **2015**, *6*, 139.
- [7] I. Roger, M. A. Shipman, M. D. Symes, *Nat. Rev. Chem.* **2017**, *1*, 0003.
- [8] C. Lohaus, A. Klein, W. Jaegermann, *Nat. Commun.* **2018**, *9*, 4309.
- [9] C. Lohaus, C. Steinert, J. Brötz, A. Klein, W. Jaegermann, *Adv. Mater. Interfaces* **2017**, *4*, 1700542.
- [10] I. S. Cho, H. S. Han, M. Logar, J. Park, X. Zheng, *Adv. Energy Mater.* **2016**, *6*, 1501840.
- [11] S. A. Carminati, A. do Nascimento Barbosa, A. L. M. de Freitas, F. L. Freire, F. L. Souza, A. F. Nogueira, *J. Catal.* **2019**, *372*, 109.
- [12] D. A. Grave, N. Yatomi, D. S. Ellis, M. C. Toroker, A. Rothschild, *Adv. Mater.* **2018**, *30*, 1706577.
- [13] N. Mirbagheri, D. Wang, C. Peng, J. Wang, Q. Huang, C. Fan, E. E. Ferapontova, *ACS Catal.* **2014**, *4*, 2006.
- [14] B. Klahr, S. Gimenez, F. Fabregat-Santiago, J. Bisquert, T. W. Hamann, *Energy Environ. Sci.* **2012**, *5*, 7626.
- [15] K. Sivula, F. Le Formal, M. Grätzel, *ChemSusChem* **2011**, *4*, 432.
- [16] C. Li, Z. Luo, T. Wang, J. Gong, *Adv. Mater.* **2018**, *30*, 1.
- [17] S. Kment, F. Riboni, S. Pausova, L. Wang, L. Wang, H. Han, Z. Hubicka, J. Krysa, P. Schmuki, R. Zboril, *Chem. Soc. Rev.* **2017**, *46*, 3716.
- [18] B. Iandolo, B. Wickman, I. Zorić, A. Hellman, *J. Mater. Chem. A* **2015**, *3*, 16896.
- [19] R. Franking, L. Li, M. A. Lukowski, F. Meng, Y. Tan, R. J. Hamers, S. Jin, *Energy Environ. Sci.* **2013**, *6*, 500.
- [20] C. A. Mesa, A. Kafizas, L. Francàs, S. R. Pendlebury, E. Pastor, Y. Ma, F. Le Formal, M. T. Mayer, M. Grätzel, J. R. Durrant, *J. Am. Chem. Soc.* **2017**, *139*, 11537.
- [21] A. Cots, D. Cibrev, P. Bonete, R. Gómez, *ChemElectroChem* **2017**, *4*, 585.
- [22] Y. Ling, G. Wang, D. A. Wheeler, J. Z. Zhang, Y. Li, *Nano Lett.* **2011**, *11*, 2119.
- [23] S. D. Tilley, M. Cornuz, K. Sivula, M. Grätzel, *Angew. Chem., Int. Ed.* **2010**, *49*, 6405.
- [24] J. Li, S. K. Cushing, P. Zheng, F. Meng, D. Chu, N. Wu, *Nat. Commun.* **2013**, *4*, 1.
- [25] E. Kecszenovity, B. Endrődi, P. S. Tóth, Y. Zou, R. A. W. Dryfe, K. Rajeshwar, C. Janáky, *J. Am. Chem. Soc.* **2017**, *139*, 6682.
- [26] E. Kecszenovity, B. Endrődi, Z. Pápa, K. Hernádi, K. Rajeshwar, C. Janáky, *J. Mater. Chem. A* **2016**, *4*, 3139.
- [27] S. Yin, X. Men, H. Sun, P. She, W. Zhang, C. Wu, W. Qin, X. Chen, *J. Mater. Chem. A* **2015**, *3*, 12016.
- [28] B. Endrődi, E. Kecszenovity, K. Rajeshwar, C. Janáky, *ACS Appl. Energy Mater.* **2018**, *1*, 851.
- [29] Y. H. Ng, A. Iwase, A. Kudo, R. Amal, *J. Phys. Chem. Lett.* **2010**, *1*, 2607.
- [30] F. Meng, J. Li, S. K. Cushing, J. Bright, M. Zhi, J. D. Rowley, Z. Hong, A. Manivannan, A. D. Bristow, N. Wu, *ACS Catal.* **2013**, *3*, 746.
- [31] A. G. Tamirat, W.-N. Su, A. A. Dubale, C.-J. Pan, H.-M. Chen, D. W. Ayele, J.-F. Lee, B.-J. Hwang, *J. Power Sources* **2015**, *287*, 119.
- [32] S. D. A. Carminati, F. L. Souza, A. F. Nogueira, *ChemPhysChem* **2016**, *17*, 170.
- [33] S. Rai, A. Ikram, S. Sahai, S. Dass, R. Shrivastav, V. R. Satsangi, *RSC Adv.* **2014**, *4*, 17671.
- [34] L. He, L. Jing, Z. Li, W. Sun, C. Liu, *RSC Adv.* **2013**, *3*, 7438.
- [35] J. Y. Kim, J. W. Jang, D. H. Youn, J. Yul Kim, E. S. Kim, J. S. Lee, *RSC Adv.* **2012**, *2*, 9415.
- [36] B. Y. Yu, S. Y. Kwak, *J. Mater. Chem.* **2012**, *22*, 8345.
- [37] J. Deng, X. Lv, H. Zhang, B. Zhao, X. Sun, J. Zhong, *Phys. Chem. Chem. Phys.* **2016**, *18*, 10453.
- [38] A. G. Tamirat, W.-N. Su, A. A. Dubale, H.-M. Chen, B.-J. Hwang, *J. Mater. Chem. A* **2015**, *3*, 5949.
- [39] J. E. Thorne, J. W. Jang, E. Y. Liu, D. Wang, *Chem. Sci.* **2016**, *7*, 3347.
- [40] W. Li, S. W. Sheehan, D. He, Y. He, X. Yao, R. L. Grimm, G. W. Brudvig, D. Wang, *Angew. Chem., Int. Ed.* **2015**, *54*, 11428.
- [41] T. H. Jeon, G. Moon, H. Park, W. Choi, *Nano Energy* **2017**, *39*, 211.
- [42] X. Guo, L. Wang, Y. Tan, *Nano Energy* **2015**, *16*, 320.
- [43] P. Peerakiatkhajohn, J.-H. Yun, H. Chen, M. Lyu, T. Butburee, L. Wang, *Adv. Mater.* **2016**, *28*, 6405.
- [44] Y. W. Phuan, M. N. Chong, T. Zhu, S.-T. Yong, E. S. Chan, *Mater. Res. Bull.* **2015**, *69*, 71.
- [45] S. R. Pendlebury, X. Wang, F. Le Formal, M. Cornuz, A. Kafizas, S. D. Tilley, M. Grätzel, J. R. Durrant, *J. Am. Chem. Soc.* **2014**, *136*, 9854.
- [46] F. Le Formal, S. R. Pendlebury, M. Cornuz, S. D. Tilley, M. Grätzel, J. R. Durrant, *J. Am. Chem. Soc.* **2014**, *136*, 2564.
- [47] Z. Huang, Y. Lin, X. Xiang, W. Rodríguez-Córdoba, K. J. McDonald, K. S. Hagen, K.-S. Choi, B. S. Brunschwig, D. G. Musaev, C. L. Hill, D. Wang, T. Lian, *Energy Environ. Sci.* **2012**, *5*, 8923.
- [48] T. Le Bahers, K. Takanabe, *J. Photochem. Photobiol., C* **2019**, *40*, 212.
- [49] O. Zandi, A. R. Schon, H. Hajibabaei, T. W. Hamann, *Chem. Mater.* **2016**, *28*, 765.
- [50] N. Mirbagheri, D. Wang, C. Peng, J. Wang, Q. Huang, C. Fan, E. E. Ferapontova, *ACS Catal.* **2014**, *4*, 2006.
- [51] R. L. Spray, K.-S. Choi, *Chem. Mater.* **2009**, *21*, 3701.
- [52] A. C. Ferrari, D. M. Basko, *Nat. Nanotechnol.* **2013**, *8*, 235.
- [53] A. M. Jubb, H. C. Allen, *ACS Appl. Mater. Interfaces* **2010**, *2*, 2804.
- [54] D. L. A. de Faria, V. S. Silva, M. T. de Oliveira, *J. Raman Spectrosc.* **1997**, *28*, 873.
- [55] J.-B. Wu, M.-L. Lin, X. Cong, H.-N. Liu, P.-H. Tan, *Chem. Soc. Rev.* **2018**, *47*, 1822.
- [56] S. Shen, S. A. Lindley, X. Chen, J. Z. Zhang, *Energy Environ. Sci.* **2016**, *9*, 2744.
- [57] G. Wang, X. Shen, J. Yao, J. Park, *Carbon* **2009**, *47*, 2049.
- [58] P. Małucha, M. Pacia, W. Macyk, *J. Phys. Chem. Lett.* **2018**, *9*, 6814.
- [59] J. Tauc, *Mater. Res. Bull.* **1968**, *3*, 37.
- [60] B. Iandolo, B. Wickman, I. Zorić, A. Hellman, *J. Mater. Chem. A* **2015**, *3*, 16896.
- [61] Y. W. Phuan, W.-J. Ong, M. N. Chong, J. D. Ocon, *J. Photochem. Photobiol., C* **2017**, *33*, 54.

- [62] P. S. G. Bassi, T. Sritharan, L. H. Wong, *J. Phys. D: Appl. Phys.* **2018**, *51*, 473002.
- [63] S. H. Aboutalebi, A. T. Chidembo, M. Salari, K. Konstantinov, D. Wexler, H. K. Liu, S. X. Dou, *Energy Environ. Sci.* **2011**, *4*, 1855.
- [64] W.-D. Zhang, B. Xu, L.-C. Jiang, *J. Mater. Chem.* **2010**, *20*, 6383.
- [65] J. G. Radich, A. L. Krenselewski, J. Zhu, P. V. Kamat, *Chem. Mater.* **2014**, *26*, 4662.
- [66] J. G. Radich, P. V. Kamat, *ACS Nano* **2013**, *7*, 5546.
- [67] A. Tsyganok, D. Klotz, K. D. Malviya, A. Rothschild, D. A. Grave, *ACS Catal.* **2018**, *8*, 2754.
- [68] D. K. Lee, K. S. Choi, *Nat. Energy* **2018**, *3*, 53.
- [69] T. W. Kim, K.-S. Choi, *Science* **2014**, *343*, 990.
- [70] K. George, X. Zhang, A. Bieberle-Hütter, *J. Chem. Phys.* **2019**, *150*, 041729.
- [71] R. Schrebler, K. Bello, F. Vera, P. Cury, E. Muñoz, R. del Río, H. G. Meier, R. Córdova, E. A. Dalchiele, *Electrochem. Solid-State Lett.* **2006**, *9*, C110.
- [72] L. M. Peter, J. Li, R. Peat, H. J. Lewerenz, J. Stumper, *Electrochim. Acta* **1990**, *35*, 1657.
- [73] L. M. Peter, *Chem. Rev.* **1990**, *90*, 753.
- [74] C. Zachäus, F. F. Abdi, L. M. Peter, R. van de Krol, *Chem. Sci.* **2017**, *8*, 3712.